Electronic Supplementary Information for:

Multi-Layer Reduced Graphene Oxide Encapsulates High-Entropy Alloy for Rechargeable Zinc-Air Batteries

*Leyi Gao[a], Xiongwei Zhong *[a], Zhitong Li[a], Junjie Hu[a], Shuyu Cui[a], Xingzhu Wang*[a], and Baomin Xu*[a]*

[a] *Department of Materials Science and Engineering, Southern University of Science and Technology, Shenzhen, Guangdong Province, 518055, China*

*Corresponding authors: Xiongwei Zhong (zhongxw@sustech.edu.cn); Xingzhu Wang (wangxz@sustech.edu.cn); Baomin Xu (xubm@sustech.edu.cn)

1. Experimental section

Chemicals and Materials

Iron chloride ($FeCl_3$, ≥ 99.9%), cobalt chloride hexahydrate ($CoCl_2·6H_2O$, 99.99%), nickel chloride ($NiCl_2$, 98%), manganese chloride ($MnCl_2·4H_2O$, 99.9%), copper sulfate ($CuSO_4$, 99.0%), urea (H_2NCONH_2, 99%), Potassium hydroxide (KOH, 95%), acrylic acid (AA, 95%), sodium hydroxide (NaOH, 96%), and ammonium persulfate (APS, ≥ 98%) were purchased from Aladdin.

1-ethyl-3-methylimidazole chloride (EMImCl, ≥ 98%) was purchased from Cheng Jie Chemical (Shanghai, China). Graphene oxide (GO, 20mg/mL) solution was purchased from MATTERENE (Shenzhen, China). The Nafion solution was bought from DuPont. Super P was bought from Canrd. Polytetrafluoroethylene (PTFE, 5wt%) was purchased from Kejin (Shenzhen, China).

Ni foam, zinc plate, carbon film, Zn wire, and stainless-steel mesh were purchased from CHAOCHUANG.

All the reagents were used as received without any further purification.

Synthesis of $Fe_6Ni_{20}Co_2Mn_2Cu_{1.5}$@rGO

To prepare the precursor solution, equal amounts of metal precursors were dissolved in deionized water at a concentration of 0.1 mol L^{-1}. These various metal salt solutions (Fe:Ni:Co:Mn:Cu) were combined in a molar ratio of 8:8:1:1:1, resulting in a mixed solution. Subsequently, 2 mL of this mixed solution and 0.02 mL 0.1 mol L^{-1} urea aqueous solution were slowly added into 25 mL 2 mg mL^{-1} graphene oxide (GO) solution and stirred magnetically for at least 30 minutes. The mixture was frozen in liquid nitrogen and then immediately transferred to a freeze-drying machine for lyophilization. The as-obtained dry powder was loaded into a graphite boat within a joule-heating machine, which was purged with inert Ar gas for high-temperature

heating. The heating process was carried out with pulse parameters set at a period of 5000 ms, a voltage of 30 V, and a current of 275 A. Temperature curves were measured using a thermal imaging camera (HIKMICRO HM-TP74H-25SVF/W/4G).

Synthesis of $Fe_2Ni_2Co_2Mn_{1.5}Cu_{1.1}$/rGO

The molar ratio of salts (Fe:Ni:Co:Mn:Cu) was adjusted to 1:1:1:1:1, the procedure remains identical to the synthesis of $Fe_6Ni_{20}Co_2Mn_2Cu_{1.5}$@rGO.

Synthesis of $Ni_{2.5}Co_{2.3}Mn_{1.4}Cu_{1.2}$/rGO

The procedure is the same as for the synthesis of $Fe_2Ni_2Co_2Mn_{1.5}Cu_{1.1}$/rGO without Fe precursor.

Fabrication of zinc-air batteries and flexible battery device

For the fabrication of homemade RZABs, the catalyst powder was grounded with Super P in a ratio of 1:1.5 wt%, and then added into ethanol with 150 μL 5 wt.% PTFE solution. The ink was mechanically grounded for 45 minutes, coated onto a carbon film, and subsequently dried under a vacuum, which served as the air cathode. The polished Zn plate was used as the anode, and a 6 mol L^{-1} KOH solution containing 0.2 mol L^{-1} $Zn(Ac)_2$ served as the electrolyte. The active area of the electrode was approximately 1.0 × 1.0 cm^2. Polarization curves were recorded using a CHI660E electrochemical workstation, and the performance of the assembled RZAB was assessed using a LAND testing system. A galvanostatic charging-discharging process with a duration of 1 hour per cycle (charging for 30 minutes, discharging for 30 minutes) was employed to

estimate the cycle life of the RZABs. The specific capacity of the RZAB was calculated based on the galvanostatic discharge curves at a current density of 10 mA cm^{-2} and the consumed mass of the Zn plate.

In the case of flexible zinc-air batteries (FZABs) devices, an optimized $Fe_6Ni_{20}Co_2Mn_2Cu_{1.5}$@rGO catalyst film coated on a stainless-steel mesh (Catalyst: Super P: PTFE= 1:1.5:1.65 wt.%) was employed as the air-cathode. Zinc wire was utilized as the anode. The discharge and charge of the FZABs devices were carried out using a LAND testing system at current densities of 2 and 5 mA cm^{-2}, with each cycle lasting 20 minutes (10 minutes for charging and 10 minutes for discharging).

Characterization

The morphological and structural analysis of the as-obtained materials were investigated using a field emission scanning electron microscope (FE-SEM; TESCAN MIRA3) and transmission electron microscopy (TEM; Talos F200X G2). X-ray diffraction (XRD) patterns were measured by a powder X-ray diffractometer (Bruke D8, Copper Kα 4 radiation, λ=1.540598 Å). The metal ion content was analyzed by an Inductive Coupled Plasma Mass Spectrometer (ICP-MS, Agilent 7700X). The Raman spectra were conducted using LabRAM HR Evolution (HORIBA, 532 nm) and obtained with an acquisition time of 20 s and accumulation of 3 times from the range of 200-2000 cm^{-1}.

Electrochemical measurements

The electrochemical catalytic measurements (Linear Sweep Voltammetry, LSV) were conducted using an electrochemical workstation (CHI 760E) with a standard

three-electrode setup at room temperature. For electrochemical performance, 20 μL of ink solution was drop-cast onto a rotating glassy carbon electrode (WE). The reference and counter electrodes were a Hg/HgO electrode in saturated KCl and a graphite rod, respectively.

The catalyst inks ($Fe_6Ni_{20}Co_2Mn_2Cu_{1.5}$@rGO, $Fe_2Ni_2Co_2Mn_{1.5}Cu_{1.1}$/rGO, and $Ni_{2.5}Co_{2.5}Mn_{1.4}Cu_{1.2}$/rGO) were prepared as follows: 2 mg of the catalyst and 40 μL of 5 wt% Nafion solution were dispersed in 360 μL of a 1:1 water/ethanol mixed solvent. For comparison, 2 mg of IrO_2, 1.5 mg of SP, and 40 μL of 5 wt% Nafion solution were dispersed in 360 μL of a 1:1 water/ethanol mixed solvent. All of these were sonicated for at least 1 hour to form a homogeneous ink solution. The OER electrocatalytic activity of the samples was assessed LSV at a scan rate of 10 mV s^{-1} at room temperature. Electrochemical impedance spectroscopy (EIS) spectra were recorded over a frequency range from 100 kHz to 0.01 Hz at an overpotential corresponding to a current density of 10 mA cm^{-2} using a Solartron SI 1260 instrument. Long-term testing of $Fe_6Ni_{20}Co_2Mn_2Cu_{1.5}$@rGO was conducted through a chronopotentiometric response in a three-electrode cell system. For this, 100 μL of ink solution was drop-cast onto a 1 cm × 1 cm Ni foam. The reference electrode was a Hg/HgO electrode immersed in saturated KCl, while a nickel (Ni) electrode served as the counter electrode. The OER performance was evaluated in an O_2-saturated 1 M KOH aqueous solution. All the measured polarization curve potentials in this work were recorded with iR compensation and subsequently converted to be referenced to the hydrogen electrode (RHE) using the equation:

$$E_{RHE} = E_{Hg/HgO} + 0.059\ pH + E^0_{Hg/HgO}\ (E^0_{Hg/HgO}=0.098V \text{ at } 25°C)$$

2. Figures

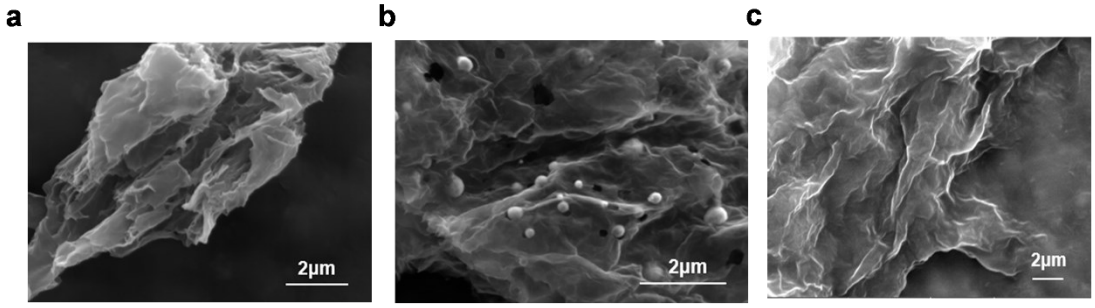

Fig. S1 (a) SEM images of $Ni_{2.5}Co_{2.5}Mn_{1.4}Cu_{1.2}$/rGO (After heating), (b) $Fe_2Ni_2Co_2Mn_{1.5}Cu_{1.1}$/rGO (After heating) and (c) $Fe_6Ni_{20}Co_2Mn_2Cu_{1.5}$@rGO (before heating), respectively.

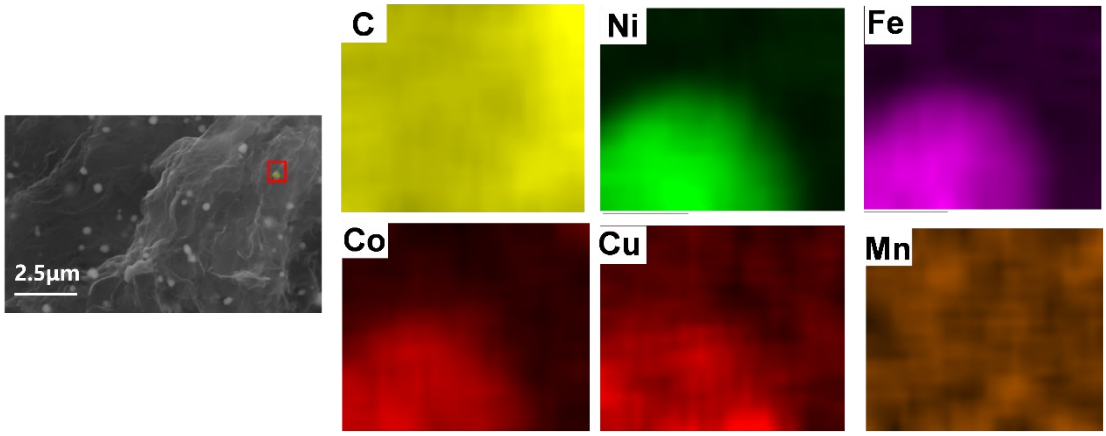

Fig. S2 SEM-EDS images of $Fe_6Ni_{20}Co_2Mn_2Cu_{1.5}$@rGO (After heating).

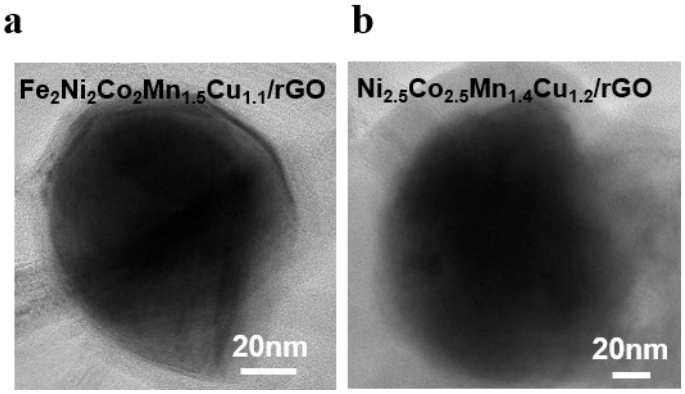

Fig. S3 TEM images of $Fe_2Ni_2Co_2Mn_{1.5}Cu_{1.1}$/rGO and $Ni_{2.5}Co_{2.5}Mn_{1.4}Cu_{1.2}$/rGO

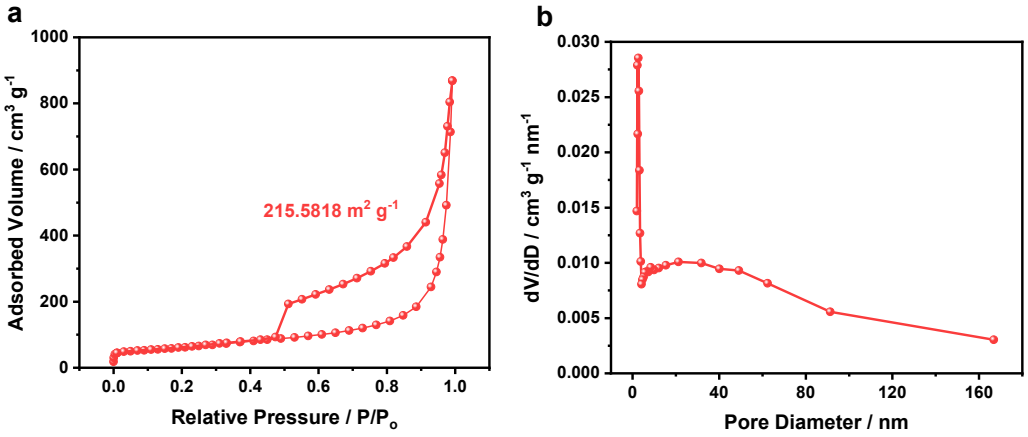

Fig. S4 (a) Nitrogen adsorption-desorption isotherm spectrum and (b) pore size distribution (PSD) curves of $Fe_6Ni_{20}Co_2Mn_2Cu_{1.5}$@rGO.

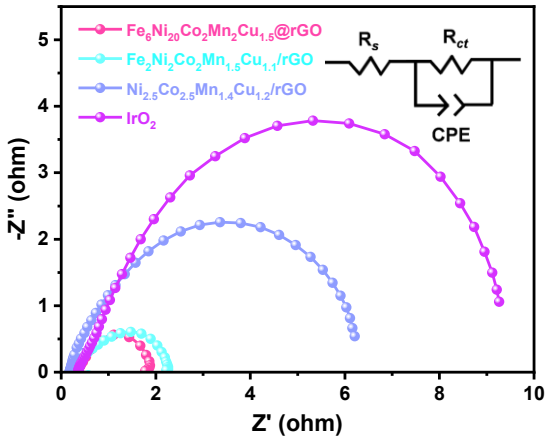

Fig. S5 EIS spectra of $Fe_6Ni_{20}Co_2Mn_2Cu_{1.5}$@rGO, $Fe_2Ni_2Co_2Mn_{1.5}Cu_{1.1}$/rGO, $Ni_{2.5}Co_{2.3}Mn_{1.4}Cu_{1.2}$/rGO, and IrO_2. Inset: the equivalent circuit of the electrochemical impedance spectroscopy (EIS). Where R_s and R_{ct} refer to the resistance of the electrolyte solution and charge transfer resistance, respectively. The constant phase element (CPE) is related to the constant phase element.

Electrochemical impedance spectroscopy (EIS) experiments were performed under OER operating conditions. The Nyquist curves and their corresponding equivalent circuits for all samples are illustrated in Fig. S5. $Fe_6Ni_{20}Co_2Mn_2Cu_{1.5}$@rGO stands out with a charge transfer resistance (R_{ct}) of 1.9 Ω, which is the lowest resistance among $Fe_2Ni_2Co_2Mn_{1.5}Cu_{1.1}$/rGO (2.3 Ω), $Ni_{2.5}Co_{2.3}Mn_{1.4}Cu_{1.2}$/rGO (6.5 Ω), and IrO_2 (9.5 Ω), underscoring its superior charge transfer capabilities.

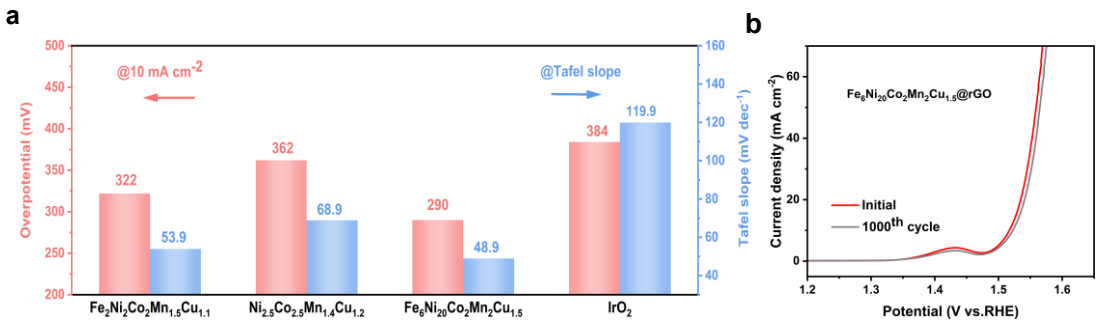

Fig. S6 (a) Summary of overpotential at 10 mA cm^{-2} and Tafel slope of catalysts. (b) The LSV curves before and after the stability test for the1000th cycle.

In a comparison of four catalysts (Fig. S6a), $Fe_6Ni_{20}Co_2Mn_2Cu_{1.5}$@rGO has the best catalytic activity (290 mV, 48.9 mV dec^{-1}), suggesting the high crystallinity reduced graphene encapsulation helps to improve OER performance. Besides, the polarization curves of the $Fe_6Ni_{20}Co_2Mn_2Cu_{1.5}$@rGO before and after 1000 cycles of stability tests almost overlap, which shows great long-term durability.

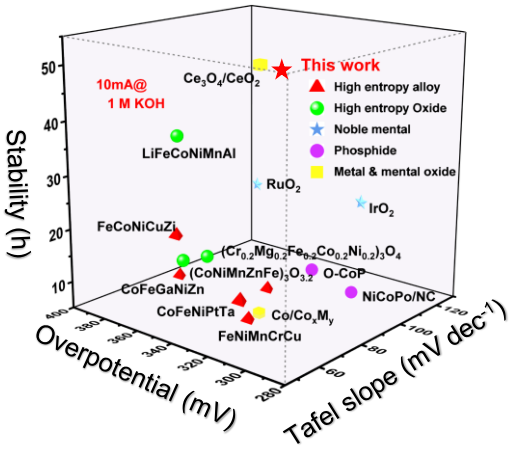

Fig. S7 (a) Comparison of overpotential, Tafel slope, and stability for $Fe_6Ni_{20}Co_2Mn_2Cu_{1.5}$@rGO and recently reported OER catalysts.

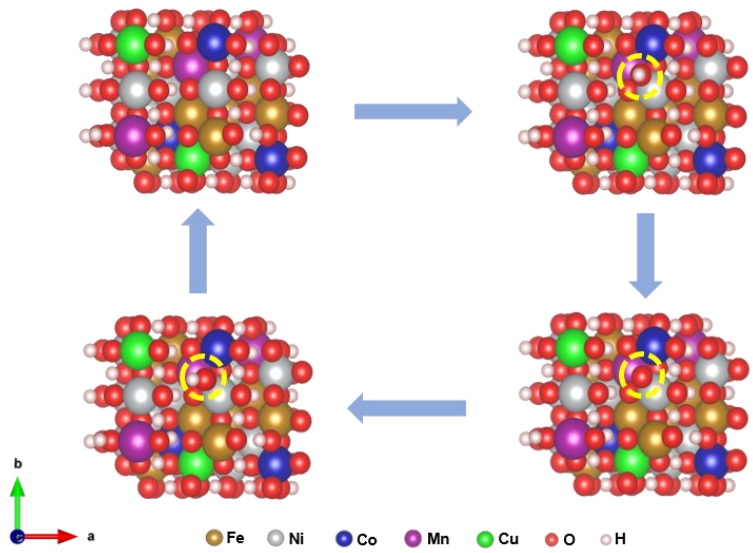

Fig. S8 DFT calculations. OER reaction mechanism on $Fe_6Ni_{20}Co_2Mn_2Cu_{1.5}$@rGO catalysts. Schematic diagram of adsorption of OH*, O*, and OOH*.

Density Functional Theory (DFT) was used to calculate the orbital hybridization overpotential and Gibbs energy barrier of the catalysts during the OER. Considering the oxidation of the HEAs surface during the OER process, for improved experimental alignment, we have constructed the HEAs model into a high-entropy hydroxide oxide model.

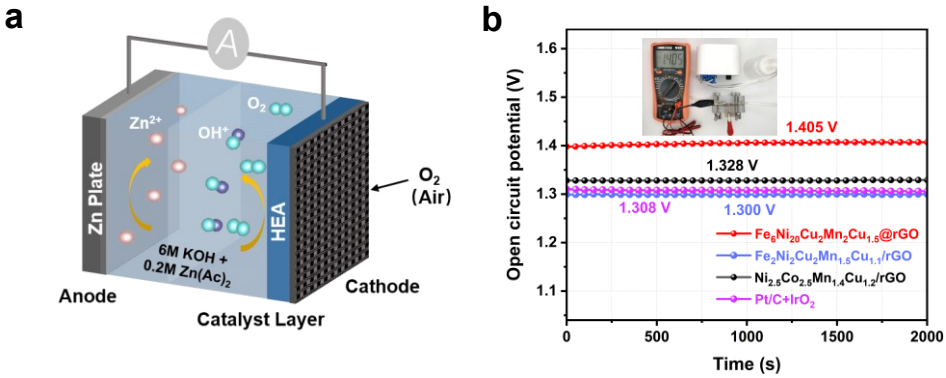

Fig. S9 (a) Schematic of the RZABs. (b) Open-circuit voltage plots of the $Fe_6Ni_{20}Co_2Mn_2Cu_{1.5}$@rGO, $Fe_2Ni_2Co_2Mn_{1.5}Cu_{1.1}$/rGO, $Ni_{2.5}Co_{2.3}Mn_{1.4}Cu_{1.2}$/rGO, and Pt/C+$IrO_2$.

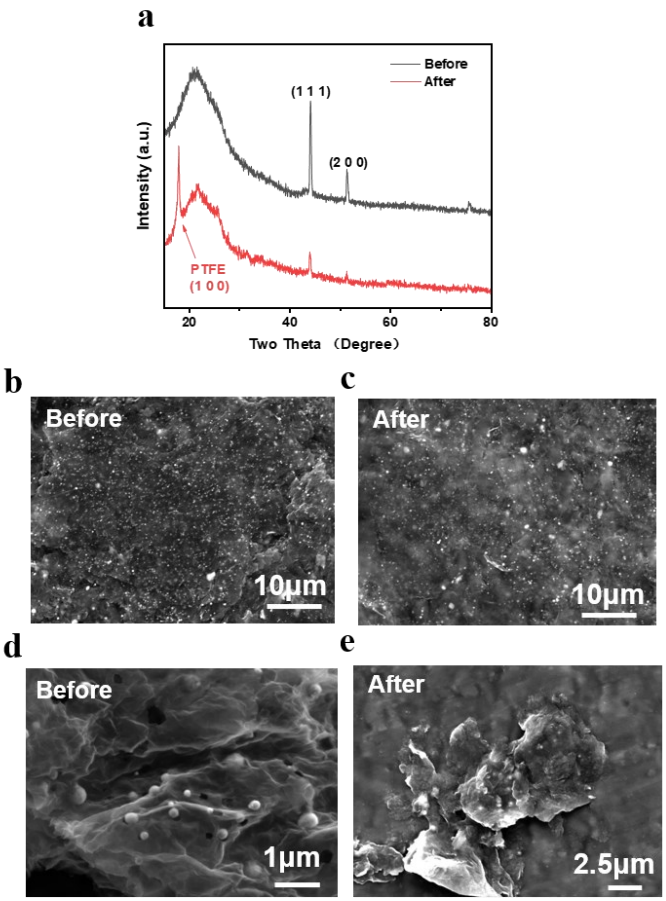

Fig. S10 (a) XRD pattern of $Fe_6Ni_{20}Co_2Mn_2Cu_{1.5}$@rGO after long-term RZAB measurements. SEM images of $Fe_6Ni_{20}Co_2Mn_2Cu_{1.5}$@rGO electrode (b) before and (c) after long-term RZAB measurements. SEM images of $Fe_6Ni_{20}Co_2Mn_2Cu_{1.5}$@rGO catalyst powder (d) before and (e) after long-term RZAB measurements.

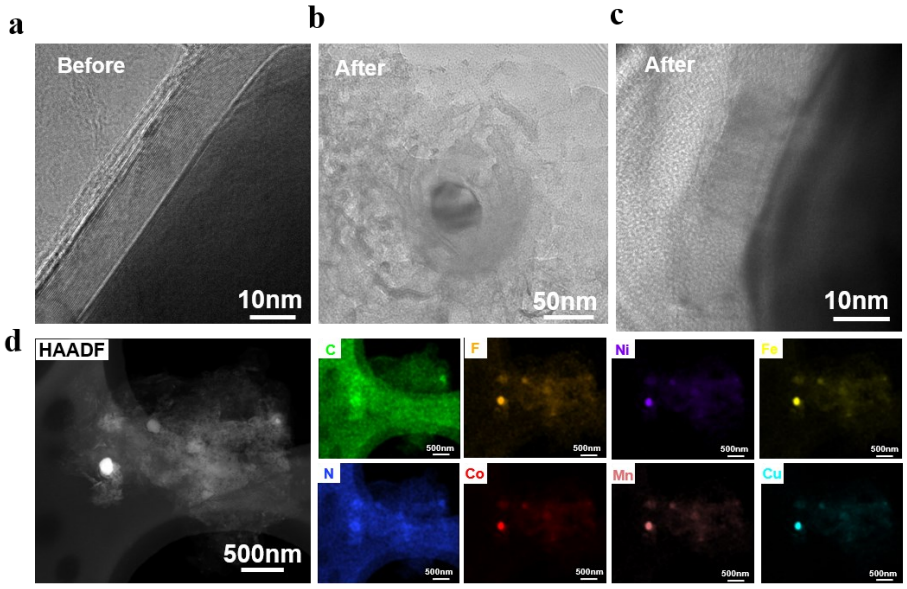

Fig. S11 TEM images of $Fe_6Ni_{20}Co_2Mn_2Cu_{1.5}$@rGO (a) before and (b, c) after long-term RZAB measurements. (d) HAADF-STEM image of $Fe_6Ni_{20}Co_2Mn_2Cu_{1.5}$@rGO and the corresponding elemental mappings after long-term RZAB measurements.

XRD analysis (Fig. S9a) shows the $Fe_6Ni_{20}Co_2Mn_2Cu_{1.5}$@rGO crystal phase does not change after the RZAB test. However, the XRD peak intensity decreased after the long-term RZAB test at 10mA cm^{-2} for 300h. Besides, it can be seen that there is a strong diffraction peak appearing around $2\theta = 18°$. This peak corresponds to the (100) crystal planes of PTFE (the reference pattern: 00-045-1594). SEM images (Figs. S9b-e) demonstrate the sustained smoothness of the electrode plates after extended cycling. TEM images (Figs. S10b-c) of $Fe_6Ni_{20}Co_2Mn_2Cu_{1.5}$@rGO after the stability test further confirmed the existence of an rGO encapsulation. The HAADF-STEM image (Fig. S10d) and corresponding X-ray energy dispersive spectrum mappings still indicate that the Fe, Ni, Co, Mn, and Cu are overlapped and all distributed on the surface of graphene.

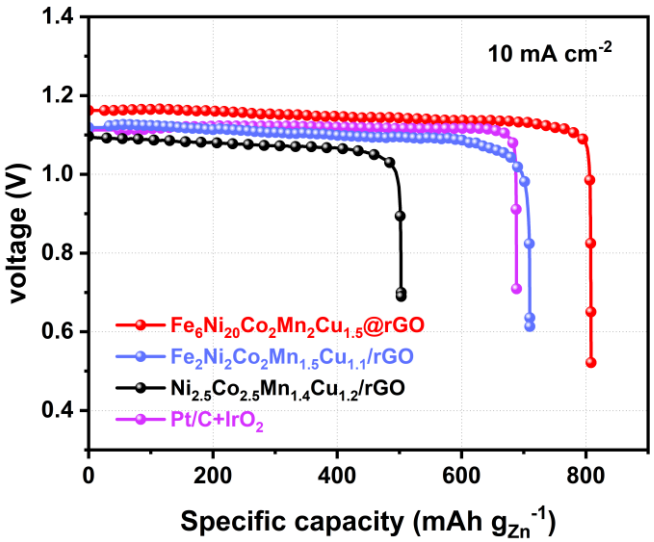

Fig. S12 Specific capacity curves of the $Fe_6Ni_{20}Co_2Mn_2Cu_{1.5}$@rGO, $Fe_2Ni_2Co_2Mn_{1.5}Cu_{1.1}$/rGO, $Ni_{2.5}Co_{2.3}Mn_{1.4}Cu_{1.2}$/rGO, and Pt/C+$IrO_2$.

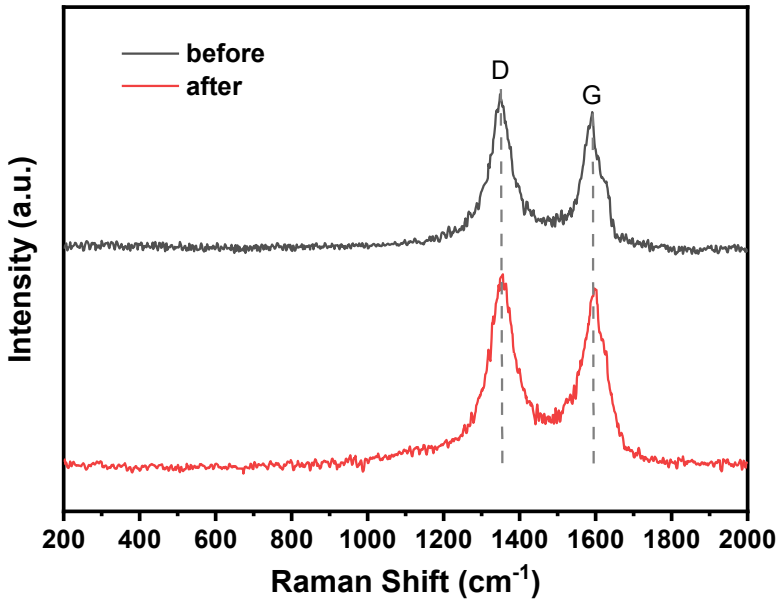

Fig. S13 Raman spectra of pristine $Fe_6Ni_{20}Co_2Mn_2Cu_{1.5}$@rGO electrode and $Fe_6Ni_{20}Co_2Mn_2Cu_{1.5}$@rGO electrode after cycling in RZAB at 10 mA cm^{-2}.

To better understand the improved mechanism of $Fe_6Ni_{20}Co_2Mn_2Cu_{1.5}$@rGO in RZAB, the Raman spectra of the electrode were carried out. The Raman spectra (Fig. S11) were obtained with an acquisition time of 20 s and accumulation of 3 times from the range of 200-2000 cm^{-1}. Regardless of whether the electrode was before and after cycling in RZAB, two peaks at approximately 1350 cm^{-1} and 1580 cm^{-1} were found, corresponding to the D and G peaks of graphene. Due to the multi-layer rGO encapsulation of HEAs, the Raman spectra exhibited very weak signals for metal peaks, and corresponding peaks were not detected in the relevant regions.

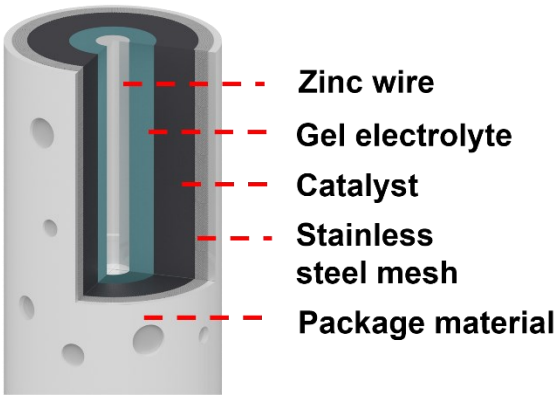

Fig. S14 Schematic diagram of FZABs.

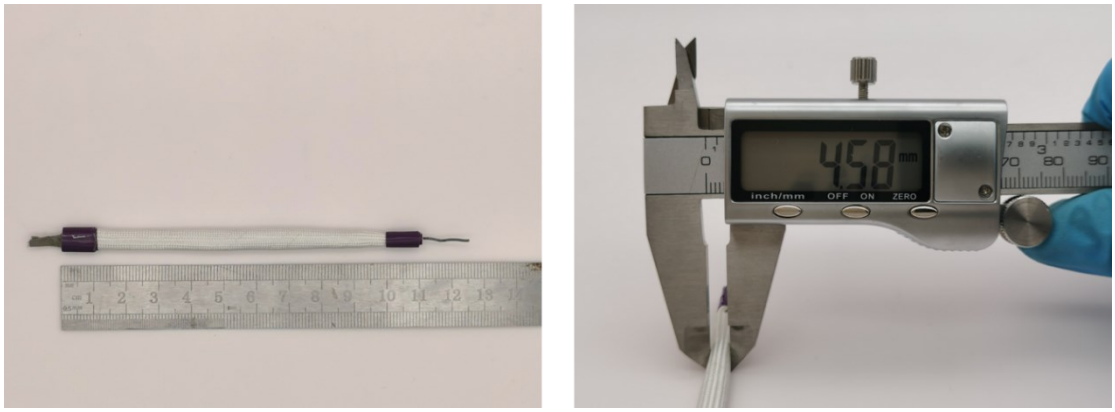

Fig. S15 Photos of the homemade 1D FZABs (Length and diameter).

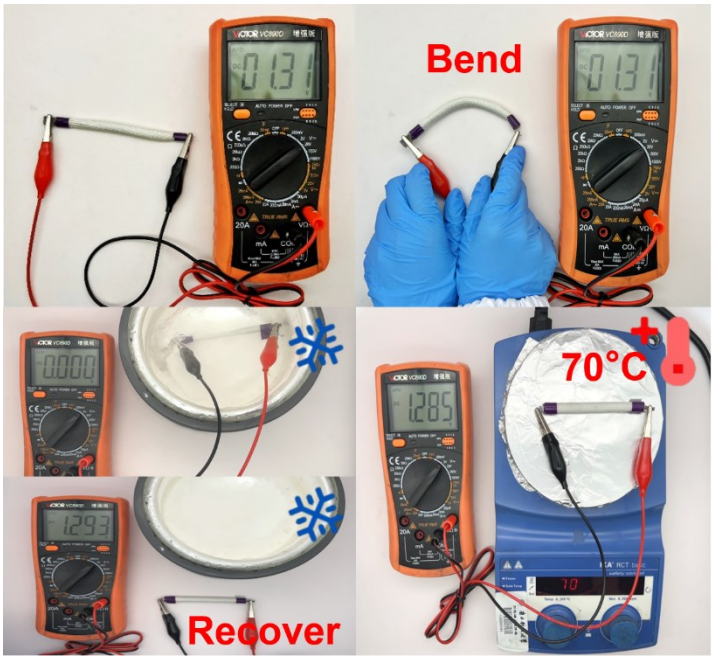

Fig. S16 OCV plots of FZABs in various conditions: room temperature, bending, freezing in liquid nitrogen, and heating.

Fig. S17 The OCV of four FZABs knitted in a woven bag.

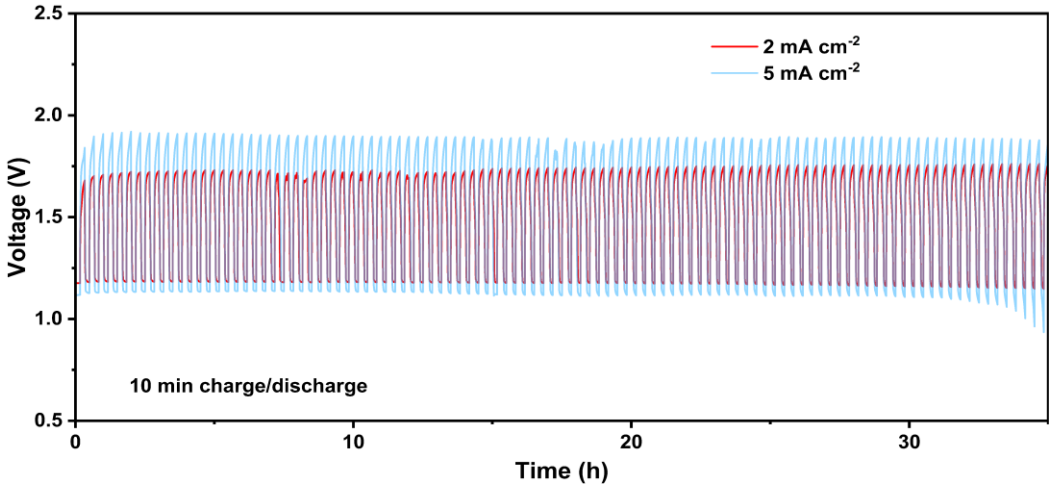

Fig. S18 The charging and discharging performance of FZAB at current densities of 2 mA cm^{-2} and 5 mA cm^{-2}.

Table S1. Summary of the Fe/Ni/Co/Mn/Cu loading for $Fe_6Ni_{20}Co_2Mn_2Cu_{1.5}$@rGO, $Fe_2Ni_2Co_2Mn_{1.5}Cu_{1.1}$/rGO, $Ni_{2.5}Co_{2.5}Mn_{1.4}Cu_{1.2}$/rGO, estimated by ICP-OES.

Sample	Fe (wt.%)	Ni (wt.%)	Co (wt.%)	Mn (wt.%)	Cu (wt.%)
$Fe_6Ni_{20}Co_2Mn_2Cu_{1.5}$@rGO	3.4631	14.1637	1.4944	0.0466	0.9672
$Fe_2Ni_2Co_2Mn_{1.5}Cu_{1.1}$/rGO	1.1710	1.1310	1.2127	0.2583	0.1953
$Ni_{2.5}Co_{2.5}Mn_{1.4}Cu_{1.2}$/rGO	——	1.4676	1.3662	0.3530	0.3727

Table S2. Summary of the specific surface area for $Fe_6Ni_{20}Co_2Mn_2Cu_{1.5}$@rGO, $Fe_2Ni_2Co_2Mn_{1.5}Cu_{1.1}$/rGO, $Ni_{2.5}Co_{2.5}Mn_{1.4}Cu_{1.2}$/rGO, estimated by BET.

Sample	Specific surface area ($m^2 g^{-1}$)
$Fe_6Ni_{20}Co_2Mn_2Cu_{1.5}$@rGO	215.5818
$Fe_2Ni_2Co_2Mn_{1.5}Cu_{1.1}$/rGO	372.4082
$Ni_{2.5}Co_{2.5}Mn_{1.4}Cu_{1.2}$/rGO	404.8132

Table S3. Comparison of the Joule heating method used in this work for the synthesis of HEA NPs with the other synthesis methods reported in the literature.

Strategies	Experimental conditions	Synthesis of HEA NPs	Substrate applicability	Duration	Refs
Joule heating	**1300 K**	**Yes**	**Carbon Substrates**	**1 min**	**/**
Solvothermal-Pyrolysis	700 K	Yes	Carbon cloth	> 5 h	[1]
Mechanical Milling	RT	Yes	Graphene	> 80 h	[2]
Wet Chemistry	973 K	Yes	Carbon	> 5 h	[3]
Liquid Metal Dealloying	> 873 K	Yes	W/O	> 5 h	[4]
Reaction Sputter Deposition	5×10^{-6} Torr	Yes	Electrodes	> 25 h	[5]

Table S4. Summary of the OER catalytic activities of $Fe_6Ni_{20}Co_2Mn_2Cu_{1.5}$@rGO HEA and recently reported other catalysts in 1.0 M alkaline electrolytes.

Sample	$\eta_{j=10}$ (mV vs. RHE)	Tafel (mV dec^{-1})	Stability (h @10mA cm^{-2})	Refs.
This work	**290**	**48.9**	**300**	**/**
FeCoNiCuZn	340	48	24	[6]
CoFeGaNiZn	370	71	10	[7]
FeCoNiCuCr	330	80	10	[8]
FeNiMnCrCu	314	58	10	[9]
CoFeNiPtTa	290	35	20	[10]
$(CoNiMnZnFe)_3O_{3.2}$	336	47.5	20	[11]
LiFeCoNiMnAl	347	53.8	40	[12]
$(Cr_{0.2}Mg_{0.2}Fe_{0.2}Co_{0.2}Ni_{0.2})_3O_4$	332	54.5	20	[13]
IrO_2	339	58	20	[14]
RuO_2	310	108	24	[15]
NiCoPO/NC	300	94	10	[16]
O-CoP	310	83.5	15	[17]
Co_3O_4/CeO_2	298	49.5	55	[18]
Co/Co_xM_y	334	79.2	5	[19]

Table S5. Comparison of the RZAB performances obtained using state-of-the-art air cathodes.

Catalyst	Peak power density (mW cm^{-2})	Specific capacity (mAh g^{-1})@ (mA cm^{-2})	Cycling durability (h)	Refs.
This work	**154.612**	**800 @10**	**300**	**/**
AlNiCoRuMo	146.5	/	120	[20]
AlFeCoNiCr	125	800 @20	120	[21]
CoZn-NC	152	578 @10	32	[22]
FeCo/NUCSs	152.35	791.86 @10	102	[23]
$FeNi_3$@NC	149.7	658 @10	280	[24]
SAC(PA+MA)	65	690.3 @5	/	[25]
Eu_2O_3-Co/NC	123.3	760.7 @5	180	[26]
CoN/CNT	173	/	100	[27]
Co@hCNTs	149	746 @10	/	[28]

Reference

1. K. Huang, B. Zhang, J. Wu, T. Zhang, D. Peng, X. Cao, Z. Zhang, Z. Li and Y. Huang, *Journal of Materials Chemistry A*, 2020, **8**, 11938-11947.
2. M. Y. Rekha, N. Mallik and C. Srivastava, *Scientific Reports*, 2018, **8**, 8737.
3. M. Liu, Z. Zhang, F. Okejiri, S. Yang, S. Zhou and S. Dai, *Advanced Materials Interfaces*, 2019, **6**, 1900015.
4. H.-J. Qiu, G. Fang, Y. Wen, P. Liu, G. Xie, X. Liu and S. Sun, *Journal of Materials Chemistry A*, 2019, **7**, 6499-6506.
5. C.-F. Tsai, P.-W. Wu, P. Lin, C.-G. Chao and K.-Y. Yeh, *Japanese Journal of Applied Physics*, 2008, **47**, 5755.
6. J. Huang, P. Wang, P. Li, H. Yin and D. Wang, *Journal of Materials Science & Technology*, 2021, **93**, 110-118.
7. L. Sharma, N. K. Katiyar, A. Parui, R. Das, R. Kumar, C. S. Tiwary, A. K. Singh, A. Halder and K. Biswas, *Nano Research*, 2022, **15**, 4799-4806.
8. R. Nandan, M. Y. Rekha, H. R. Devi, C. Srivastava and K. K. Nanda, *Chemical Communications*, 2021, **57**, 611-614.
9. X. Cui, B. Zhang, C. Zeng and S. Guo, *MRS Communications*, 2018, **8**, 1230-1235.
10. H. Chen, C. Guan and H. Feng, *ACS Applied Nano Materials*, 2022, **5**, 9810-9817.
11. Y. Zhang, W. Dai, P. Zhang, T. Lu and Y. Pan, *Journal of Alloys and Compounds*, 2021, **868**, 159064.
12. Y. Gu, A. Bao, X. Wang, Y. Chen, L. Dong, X. Liu, H. Pan, Y. Li and X. Qi, *Nanoscale*, 2022, **14**, 515-524.
13. Z. Sun, Y. Zhao, C. Sun, Q. Ni, C. Wang and H. Jin, *Chemical Engineering Journal*, 2022, **431**, 133448.
14. K. He, Z. Cao, R. Liu, Y. Miao, H. Ma and Y. Ding, *Nano Research*, 2016, **9**, 1856-1865.
15. M. Cui, C. Yang, B. Li, Q. Dong, M. Wu, S. Hwang, H. Xie, X. Wang, G. Wang and L. Hu, *Advanced Energy Materials*, 2021, **11**, 2002887.
16. C. Wang, W. Chen, D. Yuan, S. Qian, D. Cai, J. Jiang and S. Zhang, *Nano Energy*, 2020, **69**, 104453.
17. G. Zhou, M. Li, Y. Li, H. Dong, D. Sun, X. Liu, L. Xu, Z. Tian and Y. Tang, *Advanced Functional Materials*, 2020, **30**, 1905252.
18. X. Wang, M. Liu, H. Yu, H. Zhang, S. Yan, C. Zhang and S. Liu, *Journal of Materials Chemistry A*, 2020, **8**, 22886-22892.
19. J. Chen, C. Fan, X. Hu, C. Wang, Z. Huang, G. Fu, J.-M. Lee and Y. Tang, *Small*, 2019, **15**, 1901518.

20. H.-J. Qiu, G. Fang, J. Gao, Y. Wen, J. Lv, H. Li, G. Xie, X. Liu and S. Sun, *ACS Materials Letters*, 2019, **1**, 526-533.
21. G. Fang, J. Gao, J. Lv, H. Jia, H. Li, W. Liu, G. Xie, Z. Chen, Y. Huang, Q. Yuan, X. Liu, X. Lin, S. Sun and H.-J. Qiu, *Applied Catalysis B: Environmental*, 2020, **268**, 118431.
22. B. Chen, X. He, F. Yin, H. Wang, D.-J. Liu, R. Shi, J. Chen and H. Yin, *Advanced Functional Materials*, 2017, **27**, 1700795.
23. X. Xu, J. Xie, B. Liu, R. Wang, M. Liu, J. Zhang, J. Liu, Z. Cai and J. Zou, *Applied Catalysis B: Environmental*, 2022, **316**, 121687.
24. Y. Luo, D. Zhang, Y. He, W. Zhang, S. Liu, K. Zhu, L. Huang, Y. Yang, G. Wang, R. Yu, H. Shu, X. Wang and M. Chen, *Chemical Engineering Journal*, 2023, **474**, 145751.
25. K. Fan, Z. Li, Y. Song, W. Xie, M. Shao and M. Wei, *Advanced Functional Materials*, 2021, **31**, 2008064.
26. X. Wang, J. Wang, P. Wang, L. Li, X. Zhang, D. Sun, Y. Li, Y. Tang, Y. Wang and G. Fu, *Advanced Materials*, 2022, **34**, 2206540.
27. R. Xu, F. Luo, M. Li and Z. Yang, *Chemical Communications*, 2019, **55**, 13394-13397.
28. Q. Zhou, Z. Zhang, J. Cai, B. Liu, Y. Zhang, X. Gong, X. Sui, A. Yu, L. Zhao, Z. Wang and Z. Chen, *Nano Energy*, 2020, **71**, 104592.